Forward degenerate four-wave-mixing spectra of NO in the strong-field regime including polarization, line coupling, and multipole effects. II. Experiments

V. Krüger,[1] M. Dumont,[2] S. Le Boiteux,[3] Y. J. Picard,[1] F. Chaussard,[1] and B. Attal-Trétout[1,*]
[1]*Office National d'Études et de Recherches Aérospatiales, Boîte Postale 72, 92322 Châtillon Cedex, France*
[2]*Laboratoire de Photonique Quantique et Moléculaire, École Normale Supérieure de Cachan, 61 Avenue du Président Wilson, 94235 Cachan Cedex, France*
[3]*Centre de Physique Moléculaire Optique et Hertzienne, Université de Bordeaux I, 351 cours de la Libération, 33405 Talence Cedex, France*
(Received 14 July 2000; published 13 June 2001)

The behavior of forward degenerate four-wave-mixing spectra of NO $\tilde{A}$-$\tilde{X}$(0,0) in the presence of strong optical fields is observed for two crossed-polarization arrangements. The NO features in terms of coupled and isolated lines are interpreted with the complete model described in the preceding paper [V. Krüger *et al.*, paper I, Phys. Rev. **64**, 012716 (2001)]. In the intermediate regime of saturation, the variation of relative line intensities with input energy is properly reproduced for NO. Thanks to these fits, we have been able to determine saturation threshold with a good accuracy. Important properties of the different polarization schemes are observed and discussed.

DOI: 10.1103/PhysRevA.64.012717 PACS number(s): 33.20.−t, 42.65.−k, 32.80.Wr, 52.20.−j

I. INTRODUCTION

A model using a numerical solution of density matrix equations expressed in the spherical tensor formalism was proposed in paper I [1] to calculate the signal intensity of forward degenerate four-wave mixing (FDFWM). This solution is carried out assuming a particular scheme for molecular interaction that involves three-J levels and their Zeeman multiplicity. Collisional effects including the orientational contributions are taken into account in this model. The three input beams (Fig. 1) are assumed to be strong with arbitrary electric field amplitudes. Different polarization arrangements assuming linearly polarized light and parallel or crossed configurations were studied in detail throughout the parametric study of paper I. To our knowledge, this treatment is original.

Although extensive work has been performed experimentally [2–7], only few experimental investigations were carried out in saturating conditions [8–13]. In the present paper, a DFWM study of NO is undertaken experimentally in the saturation regime. Experiments are performed in a flame and the spectral fitting allows us to confirm some of the theoretical predictions of our model. The range of intermediate saturation was proved to be useful to perform quantitative measurements of concentration and it will be investigated in the present experimental study. A concentration measurement requires the preliminary knowledge of the temperature and of the signal dependence as a function of temperature in this regime. Therefore, our model is first applied to predict the variation of the DFWM signal with temperature and pressure for several saturating conditions.

The main dependence of the signal versus temperature and pressure is included in the collisional broadening parameters that are taken from separate works [14,15]. The band profile peaks at one particular J value, which is well known in the low-field limit. However, the temperature behavior of the DFWM signal is strongly depending on the level of saturation that may distort the band shapes. Therefore, our experimental level of saturation has to be precisely known in order to use the proper Rabi frequency in the theoretical calculations of the band profiles. The determination of saturation threshold is thus necessary prior to performing quantitative measurements of concentration. Once the saturation threshold is known, the effect of temperature (or pressure) is predicted using theoretical simulation of $P_{\mathrm{Sig}}^{\max}/N$: this quantity represents the coefficient relating the DFWM signal amplitude to the total number density N to be measured [1]. Quantitative concentration measurements are possible when the saturating conditions and the temperature and pressure are accurately known.

An experimental investigation of NO spectra is undertaken in a laboratory flame in which NO concentration is known and constant. The experimental setup is described in Sec. II. The effect of temperature and pressure is predicted in Section III, using the multilevel theoretical simulations. The

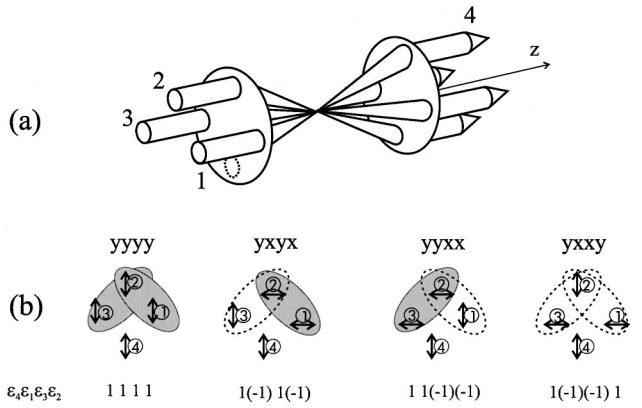

FIG. 1. (a) Beam configuration in folded BOXCARS geometry; (b) polarization arrangements and related ε_i values defined in paper I according to the labeling $\hat{\epsilon}_4\hat{\epsilon}_1\hat{\epsilon}_3\hat{\epsilon}_2$.

*Author to whom correspondence should be addressed. Electronic address: btretout@onera.fr

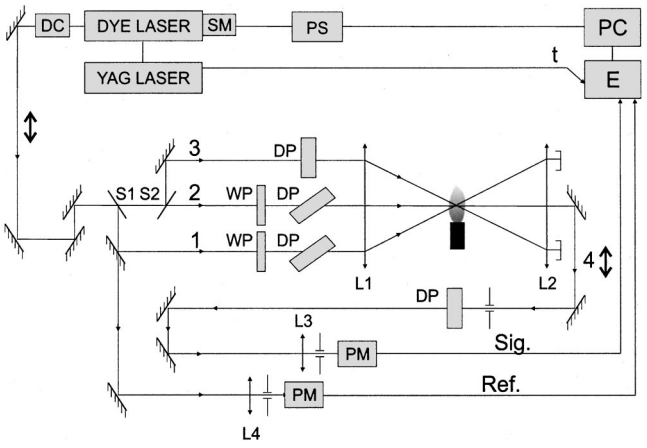

FIG. 2. Schematic diagram of the setup in the *yxyx* polarization configuration: S: beam splitter, WP: half-wave plate, DP: dichroic polarizer, L: lens, PM: photomultiplier, E: electronics, SM: stepping motor, PS: power supply of SM, DC: doubling crystal.

linewidth description is recalled. In Sec. IV, the determination of saturation threshold is first carried out by fitting experimental spectra exhibiting power broadening with adequate theoretical profiles. The influence of the polarization configuration on the line intensities and on the background level is then investigated. The validity of our model is checked and discussed.

II. EXPERIMENT

In order to validate our model, we have fitted the NO spectra recorded in a flat atmospheric pressure flame. Two different polarization arrangements are selected according to paper I [1], the *yxyx* and *yxxy* schemes of Fig. 1.

In this study, the NO spectral domain ranges from the ${}^{S}R_{21}(7.5)$ singlet (44 272.287 cm^{-1}) to the $Q_1P_{21}(17.5)$ doublet (44 266.130 cm^{-1}). The NO spectroscopic data used for the lines assignments are given in paper I [1].

A. Flame conditions

A flat premixed flame is produced on a porous plug of 60-mm diameter (McKenna Products, Inc.) at atmospheric pressure. Flow rates are 60.3 slm (standard liters per minute) of air and 10.5 slm of hydrogen, leading to lean flame conditions. A mixture of 1% NO in N_2 is added to the air flow prior to reaching the gas-mixing chamber. The 1% NO flow rate is ranging from 2 to 4 slm. The laser beams are focused 10 mm above the porous surface. The temperature is measured by CARS (coherent anti-Stokes Raman Spectroscopy) to be about 1300 K in these conditions. The seeded NO concentration is not reduced by chemical reactions in such a lean flame and is set to 400 ppm for most of our experiments.

B. Setup

The experimental setup is shown in Fig. 2. A tunable UV beam is generated by a frequency-doubled dye laser (TDL 70, Quantel) that is pumped by the third harmonic of an Nd:yttrium aluminum garnet laser (YG 782, Quantel) with a 10-Hz repetition rate. The dye laser is operated with coumarine 460 and provides pulses with energy up to 3 mJ and a linewidth of 0.12 cm^{-1} [full width at half maximum (FWHM)] at 226 nm.

The UV beam is split into three beams in a folded-Boxcars arrangement (Fig. 1). The three parallel beams are focused in the probe volume using a 890-mm focal length lens. The separation of the pump beams 1 and 3 is 22 mm leading to an angle of 1.4°. The beams are recollimated using a collection lens. Detection of the signal is performed by a UV photomultiplier tube (RTC, XP 2020 Q). The supply voltage of the PM tube is 1850 V. Spatial filtering and a dichroic polarizer are used in the coherent signal path, the generated signal is always analyzed along *y*. The pump beam 1 is polarized along *x*. The beams 2 and 3 are either polarized along *x* and *y* or *y* and *x*, to generate the *yxyx* or *yxxy* arrangements, respectively. The *y*-polarized incident beam is attenuated by a factor of 13 with neutral density filters to reduce stray light on the signal channel. Therefore the distribution of intensity of each beam is

$$I_2 = I_1, \quad I_3 = I_1/13 \quad \text{for } yxyx \text{ polarization}$$

$$I_2 = I_1/13, \quad I_3 = I_1 \quad \text{for } yxxy \text{ polarization,}$$

where I_i is the energy of beam *i* at focal volume. The attenuation factor 13 corresponds, for the field amplitude, to the reduction factor of 3.6 that has been given in paper I (Fig. 14).

In the following, the laser intensity I_{laser} refers to the energy of all beams in the focal volume, i.e., $I_{\text{laser}} = I_1 + I_2 + I_3$. For simplicity, the energy I_1 of beam 1 is given as reference in the experimental plots, with the corresponding vibronic Rabi frequency Ω_{vib1}. All these plots give the square root of the experimental FDFWM intensity, $I_{\text{DFWM}}^{1/2}$, which is directly proportional to the NO concentration.

III. TEMPERATURE AND PRESSURE STUDY

Here, our first effort is devoted to the calculation of the line-shape evolution as a function of pressure and temperature using the well-known variation of collisional and Doppler parameters versus thermodynamical conditions. The temperature and pressure dependence of the collisional widths is given by [14,15]

$$\Gamma_{ab}(k) = \frac{1}{2}\left[0.79\left(\frac{295}{T}\right)^{0.79} 0.3 + 0.585\left(\frac{295}{T}\right)^{0.75} 0.7\right] P \quad cm^{-1} \tag{1}$$

for a mixture of colliders of 30% H_2O and 70% N_2. *T* is the temperature in Kelvin and *P* the pressure in atmosphere. These linewidths are not *J* dependent in NO and are therefore the same for all the lines studied in the following discussion. The set of transversal and longitudinal widths used in our description of collisions is given in Table II of paper I. When the temperature changes, different mechanisms (Doppler and collisions) are competing in the line broadening process. These linewidths are evaluated for NO and are listed in Table I for different temperatures.

TABLE I. Spectral linewidth (HWHM) in cm^{-1} as a function of temperature (K); $P=1$ bar.

T	Collisional	Doppler	Doppler/collisional
400	0.256	0.058	0.23
600	0.188	0.071	0.38
800	0.151	0.082	0.54
1000	0.127	0.091	0.72
1200	0.111	0.100	0.90
1300	**0.104**	**0.104**	**1.00**
1400	0.098	0.108	1.10
1600	0.089	0.115	1.30
1800	0.081	0.122	1.51
2000	0.075	0.129	1.72
2200	0.070	0.135	1.95
2400	0.065	0.141	2.18

Let us recall also that we have defined a Rabi frequency in paper I, by

$$\Omega_{\alpha\beta}=\Omega_{\mathrm{vib}}(\mathrm{S}^{\mathrm{J}}_{\alpha\beta})^{1/2}, \tag{2}$$

where Ω_{vib} is the vibronic Rabi frequency and $\mathrm{S}^{\mathrm{J}}_{\alpha\beta}$ is the rotational part of the transition moment of the line under study [1].

The Doppler and collisional line widths (Table I) and their relative values as regards to Rabi broadening have a drastic influence on the final DFWM line shape. As it is well known, the temperature dependence of the signal amplitude is driven by the collisional parameters, the Doppler effect, and the thermal equilibrium of the initial population of the molecular levels. This last one is defined in paper I by

$$N_a^{(o)}=Nn_a^{(o)}, \tag{3}$$

where N is the total number density to be deduced from our experiments. $n_a^{(o)}$ is the population fraction of level $|a\rangle$ given by the normalized Boltzmann exponential as follows

$$n_a^{(o)}=\frac{e^{-E_a/kT}}{Q_vQ_R}, \tag{4}$$

where Q_v and Q_R are the vibrational and rotational partition functions and E_a is the energy of level $|a\rangle$. Both $n_a^{(o)}$ and N depend on the temperature. N varies linearly with the pressure and is inversely proportional to the temperature. Since N needs to be retrieved from the measurement of the signal intensity, the variation of $P_{\mathrm{Sig}}^{\mathrm{max}}/N$ will be calculated in different experimental conditions of pressure, temperature, and laser intensity.

According to paper I, only the ground level $|a\rangle$ is initially populated.

In the following, the behavior of the individual lines versus temperature and pressure and the envelope of the rotational band profile versus J are studied for a set of vibronic Rabi frequencies corresponding to low, intermediate and strong saturation. Let us first study the spectral profiles in the next section.

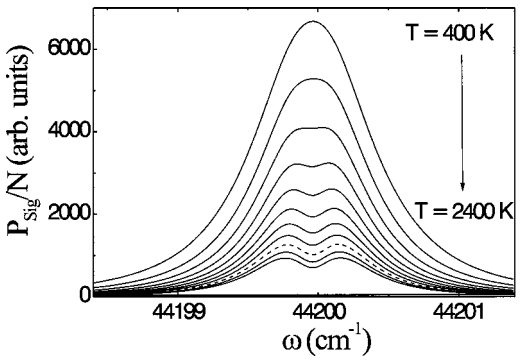

FIG. 3. Line-shape behavior vs T for $Q_1P_{21}(5.5)$ doublet in the $yyyy$ configuration with $\Omega_{\mathrm{vib}}=0.2$ and $P=1$ bar.

A. Line shapes

The calculated FDFWM line shape of $Q_1P_{21}(5.5)$ doublet is shown in Figs. 3 and 4 as a function of temperature and pressure, respectively, with $\Omega_{\mathrm{vib}}=0.2$, in the $yyyy$ configuration of Fig. 1. When temperature increases, the Doppler width increases as $T^{1/2}$ and the collisional width decreases as $T^{-3/4}$ as given by Eq. (1). In Table I, we see that collisional and Doppler widths of NO become equal to 0.104 cm^{-1} at $T=1300$ K whereas at 400 K, the collisional width dominates by a factor of 5. Conversely, at $T=2400$ K, the Doppler width is twice as large as the collision width.

As collisional contributions change, the saturation parameter also changes and is commonly defined as [16,17]

$$S_{ab}=\frac{\Omega_{ab}^2}{\Gamma_a\Gamma_{ab}}. \tag{5}$$

The saturation threshold is given by $S_{ab}=1$, which corresponds to $\Omega_{ab}^{\mathrm{sat}}=\sqrt{\Gamma_a\Gamma_{ab}}=\Omega^{\mathrm{sat}}(\mathrm{S}^{\mathrm{J}}_{ab})^{1/2}$, according to Eq. (2).

In Fig. 3, the evolution of the spectral line shape with temperature is presented under strong conditions of saturation ($\Omega_{\mathrm{vib}}=0.2$). Since Γ_{ab} decreases when temperature increases, the dip at line center, which appears at 1000 K, becomes more pronounced at 2400 K. In this case, Rabi frequency ($\Omega_{\mathrm{vib}}=0.2$) largely dominates collisional width ($\Gamma_{ab}=0.065$ cm^{-1}) and Doppler width is still too small ($\Gamma_{\mathrm{Dop}}=0.14$ cm^{-1}) to wash out this effect.

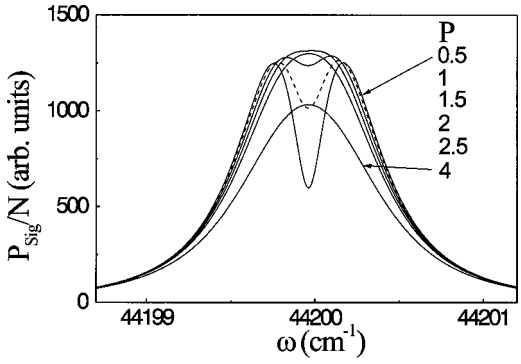

FIG. 4. Line-shape behavior vs P for $Q_1P_{21}(5.5)$ doublet in the $yyyy$ configuration with $\Omega_{\mathrm{vib}}=0.2$ and $T=2000$ K.

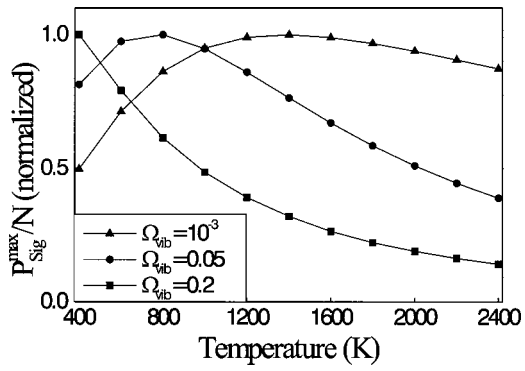

FIG. 5. Evolution of the normalized signal at line maximum for $Q_1P_{21}(5.5)$ doublet as a function of T in the *yyyy* configuration and $P=1$ bar.

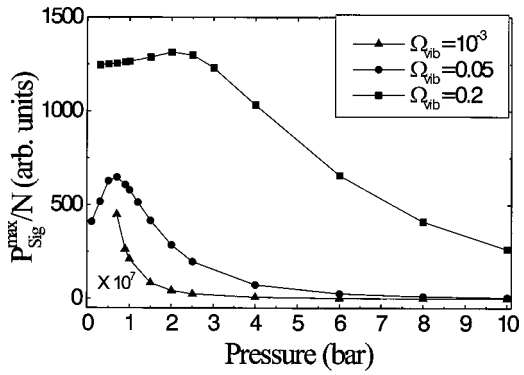

FIG. 6. Evolution of the signal at line maximum for $Q_1P_{21}(5.5)$ doublet as a function of P in the *yyyy* configuration and $T=2000$ K.

Although not taken into account here, the decrease of N with temperature may accentuate the decrease of intensity.

Pressure dependence is straightforward to interpret since it acts linearly on the collisional widths [Eq. (1)] and therefore on the final line shape (Fig. 4). Between 0.5 bar and 3 bar, the line maximum does not change significantly since the line is strongly saturated. Nevertheless, a strong modification of the line shape is observed especially at line center. At $P=2$ bar, the saturation dip vanishes and at 4 bar, the line intensity begins to decrease since collisional rates ($0.26\ \mathrm{cm}^{-1}$) become larger than the Rabi frequency. Although not taken into account in Fig. 4, the increase of N with the pressure leads to a linear increase of $P_{\mathrm{Sig}}^{\max}$.

B. Line intensity versus temperature

In Fig. 3, the line shape evolution versus temperature has been presented at high laser intensity ($\Omega_{\mathrm{vib}}=0.2$). In Fig. 5, the normalized signal amplitudes at line maximum $P_{\mathrm{Sig}}^{\max}/N$ are plotted for different input energies, as a function of temperature.

For $\Omega_{\mathrm{vib}}=0.2$, the overall effect is a marked decrease of the signal amplitude due to the combined effect of Doppler broadening and of the thermal repartition of population between levels.

Conversely, for the unsaturated case $\Omega_{\mathrm{vib}}=10^{-3}$, the signal first increases when collisional linewidth decreases and temperature grows. The signal amplitude reaches a maximum when collisional and Doppler linewidths are equal, that is around $T=1300$ K according to the data of Table I. Above this temperature, Doppler broadening becomes predominant, although collisional linewidths keep on decreasing.

For $\Omega_{\mathrm{vib}}=0.05$, the signal starts to grow from 400 K to 800 K to reach a maximum that corresponds to the saturation threshold, i.e., $T=800$ K. In this intermediate case, the decrease observed above $T=800$ K is due to stronger saturation effects.

Stronger saturation of the line implies that the maximum of the curve in Fig. 5 shifts toward lower temperature. An important remark is that around the saturation threshold, the signal dependence with T is reduced and therefore quantitative concentration measurements can be performed even when temperature is not precisely known.

C. Line intensity versus pressure

The values of $P_{\mathrm{Sig}}^{\max}/N$ are plotted in Fig. 6 as a function of pressure and for several input energies. For unsaturated conditions ($\Omega_{\mathrm{vib}}=10^{-3}$), the signal strongly decreases with pressure because the collisional broadening increases. The perturbative treatment shows a signal dependence in Γ_{ab}^{-3}. For $\Omega_{\mathrm{vib}}=0.05$ and $\Omega_{\mathrm{vib}}=0.2$, the dependence of the signal versus pressure is strongly changed and presents a maximum before a decrease. For $\Omega_{\mathrm{vib}}=0.2$, the plateau corresponds to a strong saturation regime already described in Fig. 4. Indeed, the saturation parameter is $S_{ab}=27$ for $P=2$ bar and $\Omega_{\mathrm{vib}}=0.2$ and is much higher than the saturation threshold ($S_{ab}=1$).

This plateau may allow for quantitative measurements of NO concentration disregarding the signal dependence versus pressure. In this range, the concentration is directly given by the signal amplitude whatever the pressure.

D. Line intensity versus J

The R_1Q_{21}-branch intensity is shown in Fig. 7 for $\Omega_{\mathrm{vib}}=10^{-3}$ and $\Omega_{\mathrm{vib}}=0.5$ and two temperatures $T=400$ K and $T=1200$ K. We observe a shift of the band maxima toward

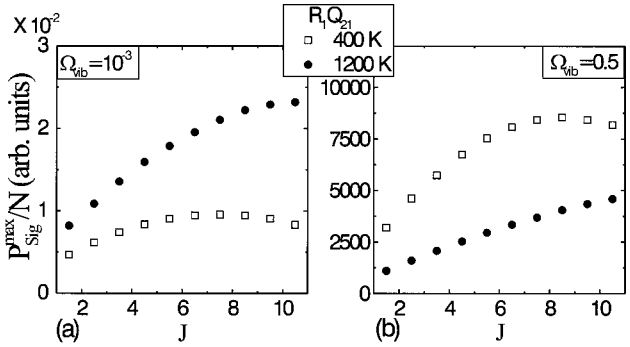

FIG. 7. Evolution of the signal at line maximum as a function of J for two different temperatures, *yyyy* configuration, $P=1$ bar in the R_1Q_{21}-branch; a: $\Omega_{\mathrm{vib}}=10^{-3}$; b: $\Omega_{\mathrm{vib}}=0.5$.

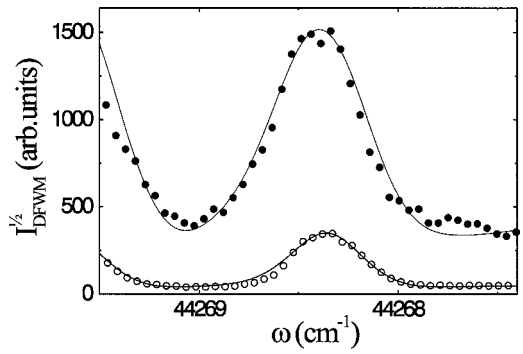

FIG. 8. FDFWM spectrum of the $Q_2R_{12}(22.5)$ doublet in *yxyx* polarization; experimental spectra with $I_1=23$ μJ (○○○) and $I_1=160$ μJ (●●●) and calculated profile (solid line) with $\Omega_{vib1}=0.06$ and $\Omega_{vib1}=0.16$, respectively.

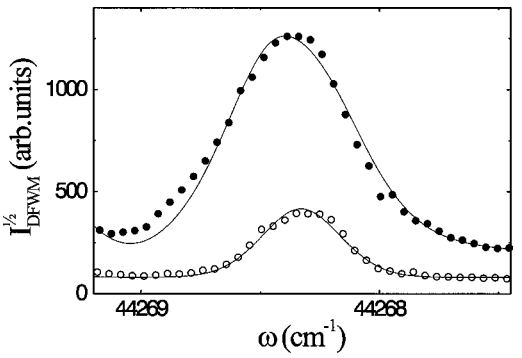

FIG. 9. FDFWM spectrum of the $Q_2R_{12}(22.5)$ doublet in *yxxy* polarization; experimental spectra with $I_1=30$ μJ (○○○) and $I_1=175$ μJ (●●●) and calculated profile (solid line) with $\Omega_{vib1}=0.07$ and $\Omega_{vib1}=0.17$, respectively.

higher J values, when the field is stronger. Thus, the amplitudes calculated at 400 K peak around $J=8.5$ when $\Omega_{vib}=0.5$ instead of $J=5.5$ at $\Omega_{vib}=10^{-3}$. At high temperature with no saturation, the J value of the band maximum also increases [Fig. 7(a)].

The temperature behavior of the band profiles has to be properly calculated in the saturation regime in order to allow accurate concentration measurements to be performed in a large gradient of temperature (turbulent flames). The theoretical predictions of the present section are used in the analysis of our experimental results.

IV. RESULTS

NO spectra have been recorded in flames for different experimental conditions. In Sec. IV A, we first establish a correspondence between the experimental laser energy per pulse and the Rabi frequency, which is the input parameter of the calculation. This correspondence is obtained by comparing the experimental and theoretical degree of saturation acting on the line shapes and the relative intensities of the different NO doublets. In fact, this adjusted Rabi frequency represents an average of the saturation over the field amplitude distribution in the interaction volume. The line fitting procedure is described in detail in Sec. IV A. In Sec. IV B, the stray-light background is phenomenologically introduced in the line-shape calculation. This background contains both coherent and incoherent parts that can interfere with the DFWM signal and distort the final line shape. In Sec. IV C, best fits of NO spectra are presented for several laser energies, polarization arrangements, and spectral regions.

A. Saturation threshold determination

The saturation process is observed on the line intensities and on the line shapes that exhibit power broadening when the Rabi frequency becomes predominant.

First, line profiles are fitted. Let us remember that the multimode structure of the laser is not taken into account in our model (paper I, Sec. II E). However, we convolve the calculated signal spectrum with the laser linewidth function, which is carefully measured experimentally [18]. This procedure is an approximation that is appropriate to our experimental conditions (laser, collisional, and Doppler widths).

The theoretical Rabi frequency corresponding to the power-broadened line is adjusted to reproduce the linewidth as shown in Figs. 8 and 9 with $P=1$ bar and $T=1300$ K as measured by CARS. The $Q_2R_{12}(22.5)$ doublet is fitted for two input laser energies and two polarization configurations. The Rabi frequencies retrieved from these fits are in good agreement. These ratios correspond to the experimental ratio of the square root of the laser energies; they are equal to $\sqrt{160/23}$ in Fig. 8 and to $\sqrt{175/30}$ in Fig. 9.

The line intensities are also studied in order to improve the Rabi frequency determination. Theoretical intensities of some lines are presented in Fig. 10 as a function of Ω_{vib1}. A better accuracy is obtained when theoretical intensity ratios (Fig. 11) are compared to the experimental ratios. These ratios are rapidly changing in the intermediate regime ($\Omega_{vib1}<0.2$), thus allowing accurate evaluation of Ω. According to this procedure, the Rabi frequency obtained from Fig. 8 is confirmed to be $\Omega_{vib1}=0.06$ for $I_1=23$ μJ (*yxyx* polarization). The linewidth comparison gives an accuracy of about 20% whereas the intensity ratios are optimized with an accuracy of less than 10%.

It appears also from Fig. 10 that for $I_1=23$ μJ, i.e., $\Omega_{vib1}=0.06$, the intermediate saturation regime starts. This value corresponds to the total intensity $I_{laser}=I_1+I_2+I_3=48$ μJ.

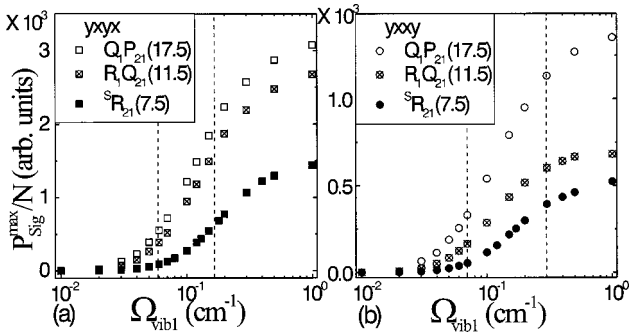

FIG. 10. Evolution of the calculated amplitude at line maximum as a function of Ω_{vib1} for $Q_1P_{21}(17.5)$ and $R_1Q_{21}(11.5)$ doublets, and $^SR_{21}(7.5)$ line in *yxyx* case (a), in *yxxy* case (b); the dashed lines indicate the domain of energy used in the experiments.

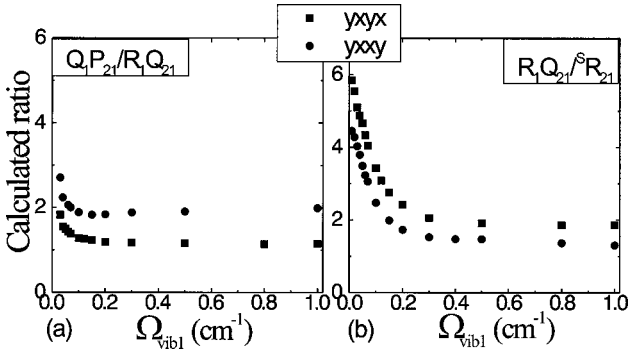

FIG. 11. Evolution of the calculated amplitude ratio of $Q_1P_{21}(17.5)/R_1Q_{21}(11.5)$ (a) and of $R_1Q_{21}(11.5)/^SR_{21}(7.5)$ (b) at line maximum as a function of Ω_{vib1} for *yxyx* and *yxxy* cases.

The same procedure is applied to the *yxxy* polarization case for $I_1=30$ μJ and 175 μJ (Fig. 9) providing $\Omega_{vib1}=0.07$ and $\Omega_{vib1}=0.17$, respectively.

Let us note that above $\Omega_{vib1}=0.2$, intensity ratios become nearly constant and are not useful anymore for the fitting procedure (Fig. 11). Here we can also notice that, in the flame at 1300 K, the saturation dip is not yet observed when $\Omega_{vib1}=0.2$. The profiles of $R_1Q_{21}(11.5)$, $Q_1P_{21}(17.5)$, and $Q_2R_{12}(22.5)$ doublets, which are scanned in our experiments, have been simulated theoretically at higher energies. At $\Omega_{vib1}=0.5$, they are found to exhibit a dip at line center (in the *yxyx* polarization arrangement). According to the above flame conditions, $\Omega_{vib1}=0.5$ corresponds to $I_{laser}=3.32$ mJ and this energy was not reached during our experiments.

B. Background interference analysis

Background interferences may distort the DFWM spectra as it was already observed on CARS spectra [19]. The background includes contributions of different nature, namely, coherent and incoherent. In our case, the coherent scattering is mainly due to thermal gratings coming from linear absorption on NO and O_2 that are present in the postflame region [20]. These contributions are assumed to be dispersive and to have a definite phase. Thermal contribution has to be added to the complex amplitude of the resonant signal under study. Furthermore, an incoherent stray-light diffusion is often observed in degenerate experiments. This contribution has a random phase and is added to the intensity of the DFWM signal.

By investigating the evolution of the background versus laser energy, we were able to discriminate the different contributions to our experimental baseline (Fig. 12). The *yxyx* and *yxxy* polarization arrangements are investigated. In the first case (*yxyx*), the background increases as the power 2.5 ± 0.1 of the laser intensity while the power dependence is 1.3 ± 0.3 in the second case (*yxxy*). In the *yxxy* case, we know that thermal grating contributions are greatly reduced since only polarization gratings are generated [21]. Therefore, the background behavior is quasilinear with the laser energy, since stray light is mainly due to the incoherent scattering of the *y*-polarized incident beam. When both thermal gratings and incoherent light are added to the background (*yxyx* polarization), it is not surprising to find a slope of 2.5 on logarithmic scale, since the coherent effect alone should exhibit a slope of 3.

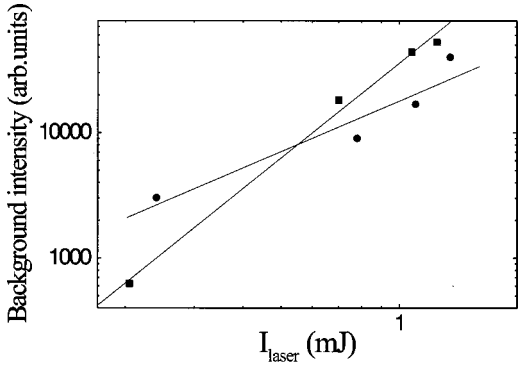

FIG. 12. Log-log evolution of the experimental background as a function of I_{laser} in the *yxyx* (■ ■ ■) and *yxxy* (●●●) cases, fitted curves (solid line) are used for power dependence determination.

In the *yxxy* case, the incoherent contribution is easily measured between two lines and simply added to the calculated original intensity. In the *yxyx* case, a part of the background is coherently added to the signal amplitude in order to represent the slight anisotropy observed on the stronger lines.

C. Spectral simulations

Figures 13 and 14 illustrate FDFWM spectra with *yxyx* polarization, for $I_1=23$ μJ and 160 μJ, respectively. For *yxxy* polarization, spectra are shown in Fig. 15 ($I_1=30$ μJ), Fig. 16 ($I_1=175$ μJ), and Fig. 17. For this last spectrum, the 890-mm focal length lens has been replaced by a 405-mm one, leading to an equivalent energy $I_1=613$ μJ.

The main difference between these spectra is the broadening, as mentioned previously, whatever the polarization arrangement. In addition, relative intensities of lines exhibit substantial changes through saturation. In the *yxyx* arrange-

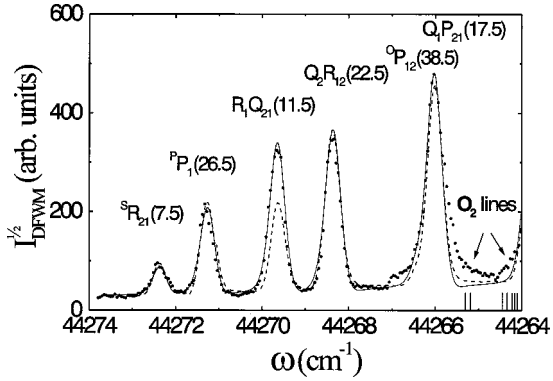

FIG. 13. FDFWM spectrum of NO in a H_2/air flame with $I_1=23$ μJ in the *yxyx* case; experimental (●●●) and simulated profile at $\Omega_{vib1}=0.06$ in the *yxyx* case (solid line) and in the *yxxy* case (dashed line).

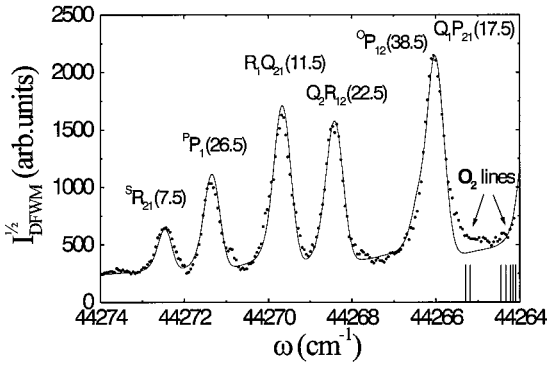

FIG. 14. FDFWM spectrum of NO in a H_2/air flame with $I_1 = 160$ μJ in the *yxyx* case, experimental (●●●) and simulated profile (solid line) at $\Omega_{vib1} = 0.16$.

ment, the $R_1Q_{21}(11.5)$ line grows compared to the $Q_1P_{21}(17.5)$ and $Q_2R_{12}(22.5)$ ones when the energy increases. Relative intensity of the $^{S}R_{21}(7.5)$ singlet line is growing since its μ_{ab} is the smallest of all the probed transitions: saturation tends to act in favor of the weakest lines. We believe the strong background between 44 264 and 44 266 cm^{-1} to arise from O_2 lines $(2,4)P(23)$, $(3,4)P(39)$, and $(4,5)R_3(17)$, which are located in this spectral range. This O_2 signal is not observed in the *yxxy* experiment; it is probably reduced and swamped by the background.

Nevertheless, comparing the different polarization arrangements, relative intensities already exhibit a different pattern in the low-energy spectra. The $Q_1P_{21}(17.5)$ and $Q_2R_{12}(22.5)$ doublets are the dominant features in both spectra, but the behavior of the $R_1Q_{21}(11.5)$ doublet is changed. In *yxyx* case, the $R_1Q_{21}(11.5)$ and $Q_2R_{12}(22.5)$ doublets have equal intensities, whereas in the *yxxy* case, $R_1Q_{21}(11.5)$ is about two times smaller than $Q_1P_{21}(17.5)$. The geometrical factors are not the only parameters responsible for that behavior since another R line, i.e., the $^{S}R_{21}(7.5)$ one, is not affected by this polarization change. Let us notice that it is an isolated line, i.e., experiencing no coupling. In opposition, the coupling between the two components of the $R_1Q_{21}(11.5)$ doublet induces an additional

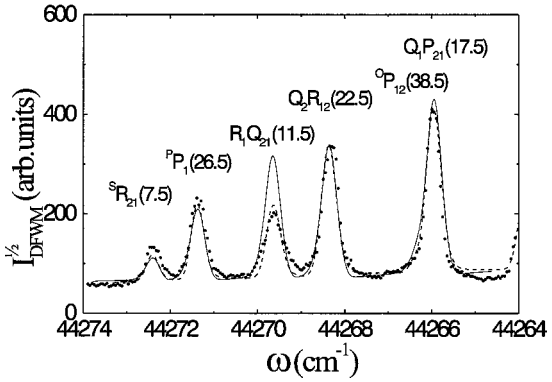

FIG. 15. FDFWM spectrum of NO in a H_2/air flame with $I_1 = 30$ μJ in the *yxxy* case, experimental (●●●) and simulated profile at $\Omega_{vib1} = 0.07$ in the *yxyx* case (solid line) and in the *yxxy* case (dashed line).

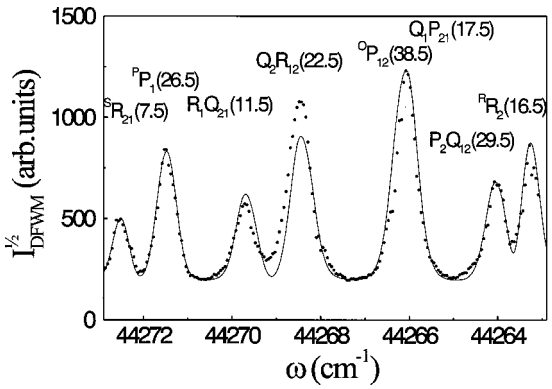

FIG. 16. FDFWM spectrum of NO in a H_2/air flame with $I_1 = 175$ μJ in the *yxxy* case, experimental (●●●) and simulated profile (solid line) at $\Omega_{vib1} = 0.17$.

effect on the final intensity, especially in the *yxxy* case, as predicted in Fig. 22 of paper I.

However, this coupling is not sufficient to explain the observed asymmetry of lines and the contribution of the coherent background has to be added as discussed previously.

V. CONCLUSION

The exact calculation of DFWM spectra is a complex task if all the important physical effects are included in the simulation. Nevertheless, we have validated our model by including a selected set of physical effects into our calculation and by comparing this numerical simulation to our experimental spectra. The calculation is time consuming but significant improvements can still be expected by changing the matrix inversion routine for more elaborate ones. Actually, the computation time is 4 h for the $^{P}P_1(26.5)$ line and 7 h for the $R_1Q_{21}(11.5)$ line on a PC (733 MHz).

The detectivity in the intermediate saturation regime is optimum. The calculation of DFWM intensities as a function of temperature and pressure is necessary to provide accurate corrections of the measured signal amplitudes in the saturation regime. The NO number density measurement requires a preliminary measurement of pressure and temperature (in our case using CARS). Then the theoretical profiles can be fitted

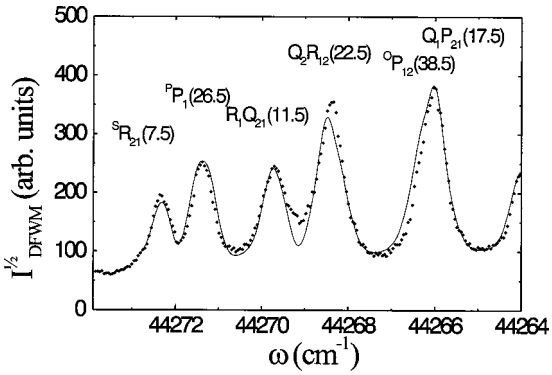

FIG. 17. FDFWM spectrum of NO in a H_2/air flame with $I_1 = 150$ μJ with 405-mm focal lens, in the *yxxy* case, experimental (●●●) and simulated profile (solid line) at $\Omega_{vib1} = 0.30$.

to the experimental ones in order to measure the saturation level and finally the number density N (assuming that the temperature and pressure factor are known). This study has demonstrated that the DFWM technique is suitable for application to real combustion engines that are currently working at high pressure and temperature. The most suitable polarization arrangement is chosen in order to provide optimum signal-to-noise ratio, minimum thermal grating contributions and, nevertheless, a sensitivity sufficient to allow trace detection in hostile environments.

The authors would like to thank P.H. Renard for his assistance in the code development and P. Bouchardy for his technical support during experiments. This work was supported in part by Direction Générale de l'Armement.

[1] V. Krüger *et al.*, preceding paper, Phys. Rev. A **64**, 012716 (2001).
[2] P. P. Radi *et al.*, Combust. Flame **118**, 301 (1999).
[3] R. L. Vander Wal, R. L. Farrow, and D. J. Rakestraw, in the Twenty-Fourth Symposium (international) on Combustion, The Combustion Institute, Pittsburgh, 1992 (unpublished).
[4] M. J. New *et al.*, Appl. Phys. B: Lasers Opt. **65**, 633 (1997).
[5] H. Latzel *et al.*, Appl. Phys. B: Lasers Opt. **67**, 667 (1998).
[6] G. J. Germann, R. L. Farrow, and D. J. Rakestraw, J. Opt. Soc. Am. B **12**, 25 (1995).
[7] V. Sick, M. N. Bui-Pham, and R. L. Farrow, Opt. Lett. **20**, 2036 (1995).
[8] S. Le Boiteux, Ph.D. thesis, Université Paris–Nord, Lab. de Phys. des Lasers, Paris, 1990 (unpublished).
[9] A. Kumar, C.-C. Hsiao, Y.-Y. Lee, and Y.-P. Lee, Chem. Phys. Lett. **297**, 300 (1998).
[10] M. S. Brown, L. A. Rahn, and R. P. Lucht, Appl. Opt. **34**, 3274 (1995).
[11] T. A. Reichardt and R. P. Lucht, J. Opt. Soc. Am. B **13**, 1107 (1996).
[12] S. Williams, R. N. Zare, and L. A. Rahn, J. Chem. Phys. **101**, 1093 (1994).
[13] T. A. Reichardt *et al.*, Appl. Opt. **38**, 6951 (1999).
[14] A. Y. Chang, M. D. D. Rosa, and R. K. Hanson, J. Quant. Spectrosc. Radiat. Transf. **47**, 375 (1992).
[15] M. D. D. Rosa and R. K. Hanson, J. Quant. Spectrosc. Radiat. Transf. **52**, 515 (1994).
[16] G. N. Robertson *et al.*, J. Quant. Spectrosc. Radiat. Transf. **55**, 71 (1996).
[17] B. Attal-Trétout *et al.*, J. Phys. B **30**, 497 (1997).
[18] Y. J. Picard *et al.*, Z. Phys. D: At., Mol. Clusters **39**, 49 (1997).
[19] B. Attal-Trétout, P. Berlemont, and J. P. Taran, Mol. Phys. **70**, 1 (1990).
[20] P. M. Danehy, P. H. Paul, and R. L. Farrow, J. Opt. Soc. Am. B **12**, 1564 (1995).
[21] S. Williams *et al.*, Opt. Lett. **19**, 1683 (1994).